Title

A High-Precision Continuous Scan and Step Scan System for Compact Spectrometer Applications

Journal

IEEE/ASME Transactions on Mechatronics, 28(6)

ISSN

1083-4435

Authors

Pyle, Kenneth E

Wu, Yen-Hung

M'Closkey, Robert T

Publication Date

2023

DOI

10.1109/tmech.2023.3265643

A high precision continuous scan and step scan system for compact spectrometer applications

Kenneth E. Pyle, Yen-Hung Wu and Robert T. M'Closkey, *Member, IEEE, ASME*

***Abstract*—A dual-stage positioning system for precisely tracking continuous scan and step scan profiles to meet the high precision dynamic positioning requirements of space optical instruments is reported. A piezoelectric walking stage provides a long-stroke platform to which a short-stroke voice coil-actuated shuttle is mounted. The shuttle corrects for sub-micrometer deviations in the walking stage position and is designed with a low resonant frequency to passively reject disturbances produced by the walking stage. Both the walking stage and shuttle are instrumented with high-resolution interferometric encoders and a feedback system regulates the shuttle's position to achieve less than 7 nm RMS position error for constant velocity references of up to 0.5 mm/s. The shuttle is also capable of tracking step scan profiles with 10 ms settling times and 1.1 nm RMS position errors for steps up to 500 nm.**

***Index Terms*—Position control, Nanopositioning, Velocity control, Vibration control, Fourier transform spectrometer**

I. Introduction

A compact system under development for mirror positioning in spaceborne Fourier transform spectrometers is proposed. The system consists of a piezoelectric-based long-stroke walking stage to which a voice coil-actuated short-stroke stage is mounted. The walking stage has a stroke of 5.2 cm and is capable of achieving nanometer-level positioning accuracy in point-to-point tasks, however, periodic contact of the piezoelectric elements that push the stage on the linear guide produce jitter while moving. The short-stroke stage is designed so that its shuttle is passively isolated from walking stage disturbances between 35 Hz and 2 kHz. A 300 Hz bandwidth feedback loop further regulates the shuttle position using a voice coil and extends the rejection of walking stage disturbances to DC. The shuttle controller also employs the walking stage lookup table input as a tachometer signal to generate sinusoidal harmonics at exactly the walking stage jitter frequencies. The harmonics are employed in a filter to eliminate periodic shuttle position errors at the selected frequencies. The shuttle passive isolation and feedback scheme collectively reduce the shuttle RMS error to 7 nm at 500 μm/s –more than a thirtyfold reduction from the walking stage error of 238 nm. Furthermore, the shuttle is also capable of step scan operation with 10 ms settling times and 1.1 nm RMS position errors for steps up to 500 nm.

The targeted application is control of the moving mirror in a Fourier transform spectrometer (FTS). The mirror is scanned up to 10 cm with velocities approaching 1 mm/s in continuous scan mode. The total stroke and velocity depend on the wavelengths to be measured. FTSs change the optical path length (OPL) of an incident signal by translating a mirror in a Michelson interferometer. As the path length is varied, constructive and destructive interference create changes in intensity at the detector: the measurement of intensity as a function of optical path length is the interferogram. The Fourier transform of the interferogram, denoted the spectrogram, reveals the spectrum of the incident signal. Additional background is provided in [1], [2].

Metrics for an FTS positioning system include sampling distance, RMS position error and mirror velocity. Requirements for four complementary wavelength bands spanning infrared to UV are provided in Table I. These metrics are briefly reviewed. The most stringent positioning requirements are determined by the shortest wavelengths to be detected. A figure of merit is to ensure the RMS error of the OPL does not exceed one thousandth of the shortest wavelength to be detected in a given band [3]. This general principle is used to specify the tolerable positioning error in Table I.

Modern instruments scan the mirror at a constant velocity and sample the interferogram with uniform increments in optical path length. When longer exposure times are required, the mirror is step scanned. The metrics in Table I are relevant to continuous-scan mode. The sampling distance defines the distance the mirror travels between consecutive detector samples. Although optical filters are used to reject shorter out-of-band wavelengths, the sampling distance must be chosen to minimize aliasing, thus, the sampling distance is band-dependent. Oversampling by 20% is typical and establishes 2.4 samples for the shortest wavelength in the band. The mirror velocity is determined by the detector sample period of 2 ms, i.e. the sampling distance must be covered in this period. Detector integration times of 1 ms are common and represent a balance between minimizing $1/f$ noise in the detector and accumulating enough photons for a reliable measurement [4]. A sample period of 2 ms allows for integration and readout and represents the most efficient use of the detector.

The total stroke for a measurement band is determined by the desired spectrogram resolution. In practice, at least one thousand cycles of the periodic interferogram are measured in order to provide adequate resolution, thus, the product of the longest wavelength to be measured by the number of interferogram periods determines the maximum OPL for a band. In other words, for the longest wavelength in Table I, an OPL of 15.2 cm is necessary, which requires a 7.6 cm mirror stroke in single-pass spectrometers.

This work was supported by a grant from the Jet Propulsion Laboratory, NASA, Award #1656585. *(Corresponding author: Robert. T. M'Closkey)*

Kenneth E. Pyle and Robert T. M'Closkey are with the Mechanical and Aerospace Engineering Department, University of California, Los Angeles, CA 90095, USA (e-mail: rtm@seas.ucla.edu). James Wu is a Staff Engineer at the Jet Propulsion Laboratory, Pasadena, CA 91109, USA.

TABLE I
FTS PERFORMANCE REQUIREMENTS

Wavelength Band	1	2	3	4
Wavelength range (μm)	0.25–0.7	0.7–2.8	2.8–8.3	8.3–15.4
Sampling distance (μm)	0.052	0.146	0.583	1.73
Mirror velocity (μm/s)	26.0	72.9	292	865
RMS Position error (nm)	0.125	0.35	1.4	4.15
Stroke (cm)	0.4	1.4	4.2	7.6

A review of existing precision positioning systems can be made in the context of the specifications in Table I. Precision positioning systems have been developed for many tasks that require nanometer-level accuracy. For example, scanning probe instruments achieve high bandwidths (10 kHz) and routinely position a lightweight probe with nanometer accuracy [5]–[11], however, the total strokes from 100 μm to several millimeters are several orders of magnitude lower than the stroke requirement of an FTS. Alternatively, feedscrew positioning systems provide long strokes [12] and have incorporated fine motion stages to improve accuracy to the nanometer level [13]. Dry bearings can be used in linear guides, however, the lubrication requirements of feedscrews is problematic for spacecraft instruments where optical components can be degraded by outgassing.

Stages based on magnetic levitation and actuation can achieve velocities in excess of 20 cm/s, possess 50 cm strokes, and achieve nanometer-level positioning errors during continuous scan profiles. Many maglev systems are under development for next generation lithography applications. Single-stage magnetically levitated systems are reported in [14]–[17]. A system capable of large displacements and rotation angles is reported in [18]. Other single-stage systems employ a hybrid strategy whereby electromagnets provide motive forces and air bearings offset gravity [19]–[21]. Maglev systems are also used in dual-stage configurations. For example, [22] reports a flexure-based fine motion platform coupled to a maglev stage that provides the long stroke. Alternatively, a linear motor/linear guide coarse motion stage supporting a magnetically levitated short-stroke stage is reported in [23] and achieves less than 10 nm RMS position errors over a 10 mm/s constant velocity scan. Magnetically levitated short-stroke stages attached to a long-stroke stage supported by air bearings are discussed in [24], [25]. Maglev-based positioning systems can meet the performance requirements of Fourier transform spectrometers, however, they are inherently multi-degree-of-freedom and require regulation of all six rigid body modes. Thus, the complexity of the sensing, actuation and control in maglev positioning systems, although justifiable for wafer lithography applications which require multi-DOF positioning capability, present too much risk for spaceborne spectrometers which only require positioning in a single degree of freedom. Furthermore, systems employing air bearings are not compatible with vacuum operation.

Single-stage positioning systems based solely on flexures have also been designed for nanopositioning tasks. The single-DOF system reported in [26] has a stroke of 8 mm with 10 nm RMS tracking error for velocities of 32 mm/s. The 2-DOF planar system in [27] has an 11×11 mm working area with a position resolution of 200 nm. These strokes are generally too short to cover the spectrum in Table I but are sufficient when only shorter wavelengths are measured.

The only reported single-stage systems that have met the stroke requirements for measurements over the entire visible spectrum are the state-of-the-art mechanisms built around a proprietary flexure-based double pendulum rotary scanner [3]. These systems are universally deployed in space optical instruments. The rotary scanner provides an OPL-to-displacement ratio of 8:1 to yield a maximum optical stroke up to 50 cm in a 30 cm by 30 cm footprint. New designs employing purely translational flexure-based scanners for optical strokes less than a few centimeters are also described and are currently used in terrestrial imaging spectrometers [28]. Unfortunately, the design details of these systems are proprietary. The translational flexure mechanisms are less costly than the double pendulum rotary scanners and are therefore a more attractive option when shorter OPL strokes are sufficient.

There is a niche for compact, lower cost, single-axis positioning systems that can be incorporated into space optical instruments and although the proposed system is tailored for spectrometer applications, this paper demonstrates how walking stages can be augmented to achieve nanometer-level motion control for complex path-following tasks. Therefore, the results may have relevance to other application areas. The novel aspects of the proposed system include the specification of a short-stroke stage whose modal properties are tailored to attenuate walking stage disturbances up to 2 kHz. A second contribution is the incorporation of the walking stage lookup table input as a time base for filters that can reject walking stage disturbances at precisely the jitter harmonics. This technique is especially effective at higher stage velocities and reduces the shuttle jitter by a factor of two beyond what is achieved through wideband feedback regulation of the shuttle position. In summary, the short-stroke shuttle experiences sixteen times less jitter than the walking stage at 1 mm/s, and over two orders of magnitude less jitter at lower velocities. Thus, these innovations produce a compact system which is capable of both continuous and step scan operation over the entire walking stage stroke.

The paper is organized as follows: Sec. II describes the proposed system and the advantages of using a low resonance shuttle (mirror location), and presents empirical frequency responses of the assembled system; Sec. III discusses the control methodology including a filter architecture for further attenuating the periodic tracking error components; Sec. IV presents experimental results for continuous scan and step scan modes; Sec. V discusses the experimental results in the context of FTS applications; Sec. VI concludes the paper.

II. System description

Existing systems with sufficient stroke are capable of point-to-point positioning with nanometer-level accuracy, however, with the notable exception of the current double pendulum design in existing FTSs [3], all existing long-stroke systems that

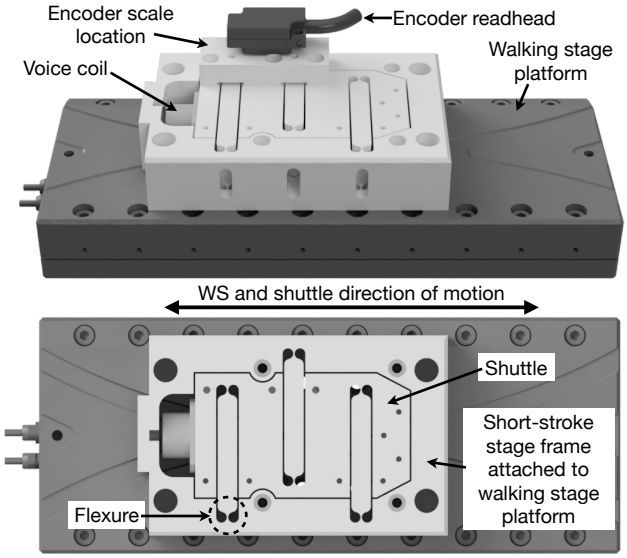

Fig. 1. **Top:** Dual-stage system consisting a walking stage with a 5.2 cm stroke to which the frame of the short-stroke stage is mounted. The encoder readhead and walking stage base are fixed to the same optical bench. An encoder scale is mounted to the shuttle of the short-stroke stage so the shuttle position is read out by the encoder. A voice coil exerts forces between the shuttle and the short-stroke stage frame. **Bottom:** Top view of system. The readhead, encoder scale mounting fixture and spars to stiffen the shuttle have been removed to clearly show the shuttle, short-stroke stage frame and thin flexures and beams which permit limited motion of the shuttle relative to the frame.

can meet the FTS position error requirements under continuous scan operation have employed a dual-stage mechanism. The proposed system is also a dual-stage mechanism, however, the fine motion stage is specifically engineered to mitigate position perturbations introduced by the long-stroke stage.

A. Long-stroke stage

The proposed system is shown in Fig. 1. A walking stage (WS) can meet the stroke and average velocity requirements for the spectrometer and is selected over a direct drive linear motor because of its intrinsic stiffness and ability to hold position without power. Furthermore, a walking piezo actuator is already a proven technology in Fourier transform spectrometers as it has been successfully deployed as the long-stroke actuator in a flexural guided terrestrial FTS in step scanning mode [28]. For continuous scan operation, though, a WS must be supplemented by a short-stroke stage to correct for WS positioning errors –this discussion is deferred to Sec. II-B.

A Physik Instrumente N-565 walking stage is selected as the long-stroke stage and although its 5.2 cm stroke does not completely cover the requirements of Band 4, this stage is suitable for demonstrating the efficacy of a dual-stage mechanism incorporating a WS. The walking stage is equipped with a 0.5 nm resolution integrated encoder that measures the WS platform position relative to the supporting optical bench. Two sets of bimorph piezoelectric legs are controlled with four voltages that specify the clamping and feed associated with each set of legs. The voltage profiles are specified via a lookup table (LUT) whose input is a non-dimensional phase. The LUT can be interpreted as defining one period of a periodic function, so a modulo operation is implemented at the input of the LUT. One period corresponds to the phase interval $[0, 1000]$. The LUT values are based on those proposed in [29] and are adapted to the voltage range of the piezoelectric elements in the WS. One pass through the LUT moves the WS approximately 8 μm so the number of LUT cycles per second for an average velocity of v_0 (in μm/s) is approximately $v_0/8$ Hz. The lowest frequency mode of the walking stage is approximately 800 Hz. These specifications are summarized in Table II.

TABLE II
SYSTEM SPECIFICATIONS

	Long-stroke stage	Short-stroke stage
Principle	PI N-565 walking stage	Flexure-based
Measurement	Built-in encoder, 0.5 nm resolution	Celera encoder, 1.2 nm resolution
Actuation	4 channels of piezo voltages via LUT	Sensata voice coil
Stroke (mm)	52	0.5
L-W-H (mm)	$160 \times 65 \times 20$	$82 \times 55 \times 17$
First resonance	800 Hz	24 Hz

The clamping and feed of the legs in a walking stage are coordinated to advance the stage on a linear roller guide. Although the stage's point-to-point performance is well-matched to step scanning applications, the periodic contact of the legs produces large position errors under continuous scan operation [29]. The WS position errors can be somewhat mitigated by carefully designing the voltage profiles that control the feed and clamping of the piezoelectric elements and/or by equalizing the variation in local gain as the legs complete one "phase" of motion [30], but there appear to be limits on what can be achieved –an RMS error of 200 nm is reported in [30] for a mean stage velocity of 1 mm/s after careful optimization of the WS controller. The walking stage position errors in the proposed system corresponding to average velocities of $v_0 = \{100, 1000\}$ μm/s are shown in Fig. 2. The power spectral densities (PSDs) of the tracking errors are also shown and exhibit fundamental frequencies corresponding to approximately $v_0/8$ Hz with numerous harmonics. Considerable variation about the ramp position reference is apparent.

B. Short-stroke stage

Fine motion control is achieved in the shuttle of the short-stroke stage that is attached to the WS. The short-stroke stage, also shown in Fig. 1, consists of a frame that supports an inner shuttle via three sets of thin flexures. The frame is fixed to the WS platform and the flexures permit collinear translational motion of the shuttle relative to the WS translation. The flexures are designed to produce a shuttle resonant frequency as low as practicable while still providing adequate support for the shuttle payload. This design passively mitigates the position disturbances generated by the walking stage that are transmitted to the shuttle –the passive isolation is quantified in Sec. II-C. This approach was also successfully applied to isolate a metrology platform attached to a gantry robot, see [31], [32]. In addition to the passive isolation, the shuttle is also

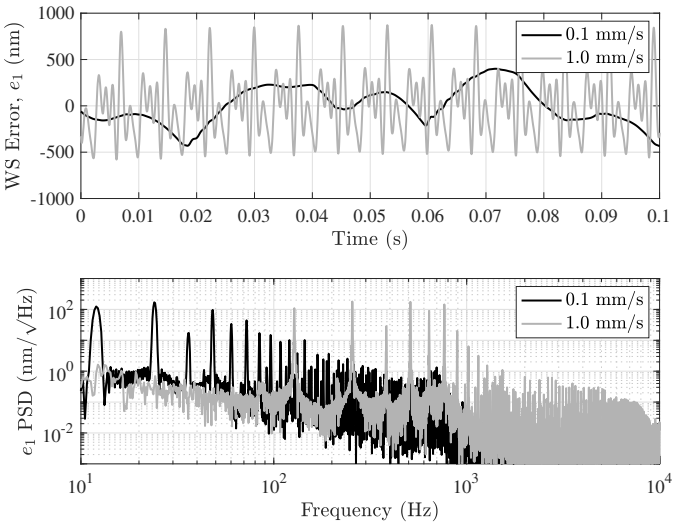

Fig. 2. **Top:** Walking stage position errors relative to ramp position references $r(t) = v_0 t$, $v_0 = \{0.1, 1\}$ mm/s. The RMS errors are about 200 nm and 328 nm, respectively. **Bottom:** Power spectral densities of the position errors. The fundamental frequencies are approximately 12.5 Hz and 125 Hz when $v_0 = 0.1$ and 1 mm/s, respectively.

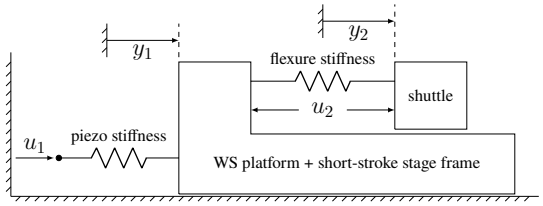

Fig. 3. A simplified representation of the system in Fig. 1 showing the relations between the input and output signals. The shuttle position, y_2, is measured by the readhead shown in Fig. 1. The walking stage position, y_1, is measured by an encoder internal to the stage.

actuated by a voice coil (VC) to further reject disturbances to its position. A VC is selected because it does not increase the elastic coupling between the frame and shuttle. For example, with a piezoelectric stack actuator, the position errors of the WS would be transmitted to the shuttle over a broad frequency band via the stiff piezoelectric elements. In comparison, the proposed flexure-based design reduces walking stage disturbances from 34 Hz to 2 kHz. When augmented by feedback regulation of the shuttle position, disturbance rejection from DC-2 kHz is achieved in the proposed system.

The shuttle is instrumented with an optical interferometric encoder, see Table II. The encoder readhead is mounted to the optical bench that supports the walking stage base so that the shuttle encoder measures the shuttle position relative to the optical bench. The voice coil actuator exerts forces between the shuttle and the short-stroke stage frame. The shuttle typically moves less than 1 μm relative to the frame for the experiments described in Sec. III although the gaps permit 0.5 mm of travel. The lowest frequency mode of the shuttle is its translational mode at approximately 24 Hz.

The two degree-of-freedom model of the dual-stage system in Fig. 3 is useful for interpreting the relationships between the inputs and measurements. In this figure and the physical system y_1 and y_2 represent the walking stage and shuttle

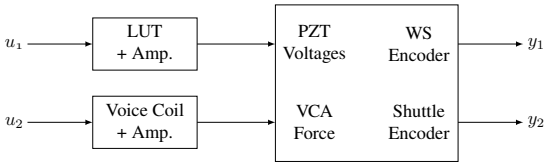

Fig. 4. Block diagram of the two-input/two-output dual-stage system, P. The system is attached to an optical table and y_1 and y_2 are the walking stage and shuttle positions, respectively, relative to the table.

positions with respect to ground (the optical bench where the assembly is tested). The input u_1 in Fig. 3 represents the position of the free end of a spring that models the piezoelectric leg stiffness. This is a reasonable analogy for the physical system where u_1 is the LUT input because the walking stage will have constant average velocity when $\dot{u}_1$ is constant. The second input, u_2, is the voltage reference applied to voice coil amplifier, however, in Fig. 3 it represents the force exerted between the shuttle and WS. Nevertheless, this model shows that the frequency responses of y_1 and y_2 with respect to u_1 are equal at low frequencies and that u_2 has no effect on the DC value of y_1 because it is an internal force between the walking stage and shuttle. These properties are confirmed in Sec. II-C. It is also possible to achieve arbitrary DC values of y_1 and y_2 by appropriate specification of u_1 and u_2, although in the physical system the deviation of y_2 from y_1 is limited by the shuttle stroke.

C. Open-loop frequency response

Testing is performed with a dSpace DS1104 DSP that interfaces to the encoders, piezo voltage amplifiers, and voice coil amplifier. A DAC drives the VCA buffer with 16b resolution over a ± 0.5 V full-scale range. The LUT is implemented in the DSP and specifies the piezo driver outputs with 16b resolution over the -10 V to 45 V range associated with the walking stage piezoelectric elements. The sample rate is 20 kHz for all experiments and all data are reported over the full measurement bandwidth (DC-10 kHz) with no post-measurement filtering. The frequency response estimates given below are from the perspective of the discrete-time controller implemented in the DSP and include the dynamics of the encoder anti-alias filters, the hold operation on DACs, and the dynamics of the VCA and piezo voltage drivers.

The frequency responses of the proposed system relate the physical input variables $\{u_1, u_2\}$ to the output variables $\{y_1, y_2\}$ –see the block diagram in Fig. 4. Individual channels of the two-input/two-output plant, P, are labeled $P_{11} = y_1/u_1$, $P_{21} = y_2/u_1$, etc. A handful of small-signal models are identified about nominal LUT phases, denoted ϕ_0, for both the u_1 and u_2 inputs. The LUT input is $u_1 = \phi_0 + \delta$, where δ represents the dither signal that is used for testing. The stimulus signals used for identification are broadband, Gaussian signals. Standard spectral estimation is used to produce the empirical frequency responses. The estimates with the LUT dither input are shown in Fig. 5. Four different values for ϕ_0 are selected to illustrate the variations in the WS dynamics. The dual-stage system is dominated by two modes near 24 Hz

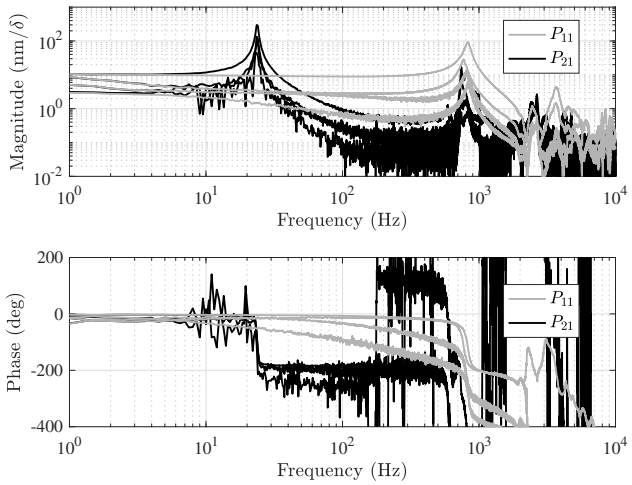

Fig. 5. Magnitude and phase of the empirical frequency responses with a dither signal, δ, on the LUT input measured about four nominal phases, ϕ_0 ($u_1 = \phi_0 + \delta$). The small-signal responses are dependent on ϕ_0, however, P_{21} and P_{11} and can be paired for different nominal phases because $P_{21} = P_{11}$ below 10 Hz.

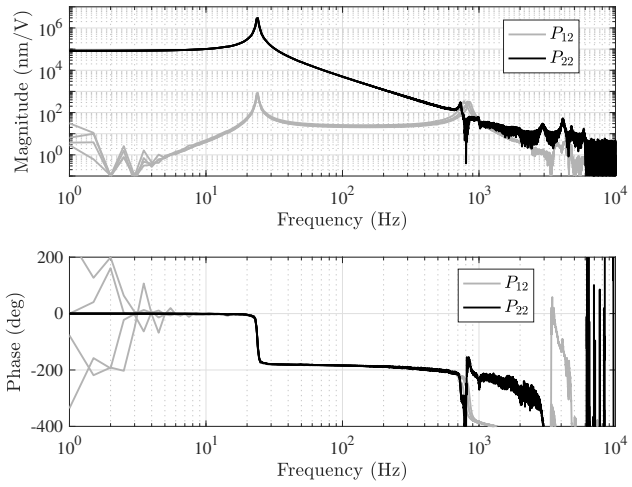

Fig. 6. Magnitude and phase of the empirical frequency responses with the voice coil input at the same four nominal LUT phases. The shuttle response to the VCA (P_{22}) is essentially independent of ϕ_0.

and 800 Hz, corresponding to the shuttle mode and WS mode, respectively, which remain virtually unchanged in frequency when the short-stroke stage is mounted to the WS. It is evident that the small-signal models for the walking stage and shuttle with respect to u_1 are highly dependent on ϕ_0. This nonlinear behavior is well-documented in walking stages and contributes to jitter when moving [29].

The frequency response estimates of the dual-stage system with the voice coil input, shown in Fig. 6, demonstrate that the VC-to-shuttle frequency responses are essentially independent of the LUT phase. Isolation of the shuttle from the WS platform is demonstrated using the system's open-loop frequency responses. A disturbance applied at u_1 moves both the WS and shuttle. The magnitude of P_{21}/P_{11} determines if the shuttle attenuates or amplifies the deviations in the WS position. The magnitude of P_{21}/P_{11} is shown in Fig. 7 for a single LUT phase, however, it is essentially independent of

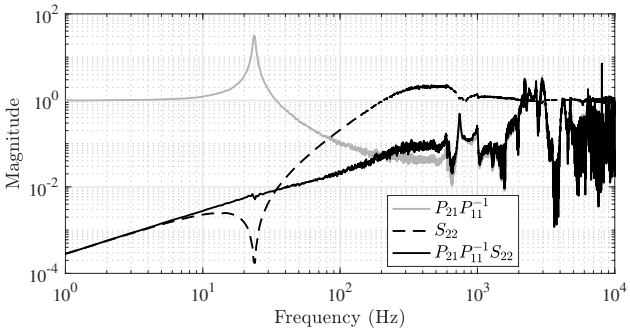

Fig. 7. In open-loop, P_{21}/P_{11} demonstrates that perturbations to the shuttle position due to walking stage jitter is attenuated from 34 Hz to over 2 kHz. S_{22} demonstrates how general disturbance forces acting on the shuttle are rejected by the shuttle loop. In closed-loop, $(y_2/d_1)/(y_1/d_1) \approx (P_{21}/P_{11})S_{22}$ shows that perturbations to the shuttle position due to walking stage jitter is attenuated from DC to over 2 kHz. Thus, the shuttle loop sensitivity function, S_{22}, scales the open loop ratio P_{21}/P_{11} to yield the closed-loop transmission from the WS position to the shuttle position.

ϕ_0. Since $|P_{21}/P_{11}| < 1$ for frequencies between 34 Hz and 2 kHz, passive attenuation of the shuttle position from walking stage jitter is achieved over this frequency band. This graph also demonstrates that the shuttle displacement follows the WS displacement below 10 Hz because $P_{21}/P_{11} \approx 1$, however, in a neighborhood of the shuttle mode near 24 Hz, WS position disturbances are amplified. Finally, in view of the 16b, ± 0.5 V range for u_2, the low frequency magnitude of P_{22} yields a DC position sensitivity of 1.27 nm/b.

III. Controller

The walking stage stage provides the long-stroke capability of the dual-stage system and also establishes a constant average velocity of the shuttle for continuous scan trajectories. The short-stroke stage corrects for walking stage jitter and other disturbances which may act on the shuttle. Due to the difficulty of eliminating the WS jitter, the WS input u_1 is also unsuitable for regulating the shuttle position, y_2, beyond the task of moving the shuttle at the desired average velocity. Furthermore, since the objective of the dual-stage system is to provide low tracking error in the shuttle position, there is little to be gained by using the VCA input, u_2, to control the WS position, y_1. Thus, from the perspective of controlling the position variables, there is no compelling reason to close loops from y_1 to u_2 and from y_2 to u_1. This suggests a diagonal controller for the two-input/two-output plant,

$$C = \begin{bmatrix} C_{11} & 0 \\ 0 & C_{22} \end{bmatrix}. \tag{1}$$

The closed-loop system is shown in Fig. 8. The discussion of C_f is deferred to Sec. III-D. The position reference, r, is provided to both the walking stage and short-stroke stage controllers. The WS and shuttle tracking errors are denoted e_1 and e_2, respectively. Disturbances at the plant input are denoted d_1 and d_2, where d_1 can be used to model disturbances that cause WS jitter and d_2 models disturbances that act on the shuttle like gravitational forces and accelerations due to slewing/repositioning the spectrometer. The closed-loop transfer function $y/d = P(I + CP)^{-1}$ determines how these

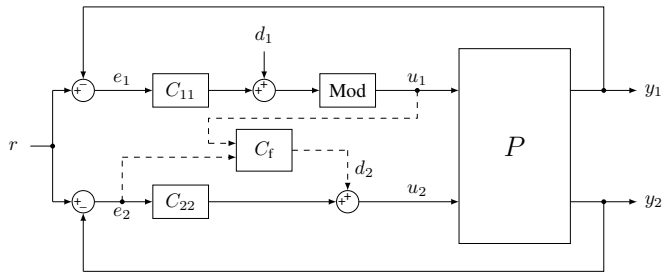

Fig. 8. Closed-loop block diagram. The "Mod" block implements a "floored division modulo" operation that converts the output of C_{11} into an appropriate LUT phase in the interval $[0, 1000]$. The LUT input, u_1, is used as a time base in $C_{\rm f}$ for generating sinusoidal signals at the frequencies of the periodic error components in e_2.

disturbances effect the WS and shuttle positions. Individual channels of y/d are denoted y_1/d_1, y_2/d_1, y_1/d_2, and y_2/d_2. Let $S_{11} = (1 + P_{11}C_{11})^{-1}$ and $S_{22} = (1 + P_{22}C_{22})^{-1}$denote the sensitivity functions associated with the "walking stage loop" and "shuttle loop", respectively. In view of the frequency responses in Figs. 5 and 6, because $|P_{12}P_{21}/(P_{11}P_{22})| \ll 1$ for frequencies less than 750 Hz it can be shown y/d is closely approximated by

$$y/d = \begin{bmatrix} P_{11}S_{11} & P_{12}S_{11}S_{22} \\ P_{21}S_{11}S_{22} & P_{22}S_{22} \end{bmatrix}, \qquad (2)$$

independent of the controller. This expression shows that the disturbance-to-position transmission in the two-input/two-output system is determined by the "single loop" sensitivity functions S_{11} and S_{22}. Since the focus is on reducing disturbance coupling to the shuttle position, the control design strives to reduce the magnitude of the second row of transfer functions in (2), thus, C_{11} and C_{22} are designed to shape S_{11} and S_{22}, respectively.

A. Walking stage compensator, C_{11}

The dependency of P_{11} on the nominal LUT phase, ϕ_0, reveals the challenge of designing a high bandwidth controller for the WS: the magnitude and phase are highly dependent on ϕ_0. Despite the nonlinear behavior of the WS one can conclude based on the PSDs in Fig. 2 that the stage resonance near 800 Hz does not appear to be a major contributor to the WS tracking error spectra in Fig. 2. Thus, there is no need to dampen the WS resonance. In consideration of the highly variable WS dynamics, a robust approach to obtaining constant velocity is to use a relatively low bandwidth controller. Thus, a compensator of the form $C_{11} = K(s + z)/s^2$ is designed for the walking stage in which the zero, z, is located at about 0.3 Hz, and K is chosen so that the gain crossover of $P_{11}C_{11}$ is between 1 and 4 Hz for the small-signal models. The controller frequency response is shown in Fig. 9 and the corresponding loop gain $P_{11}C_{11}$ is shown in Fig. 10. Although the controller is given in continuous-time form, the controller is discretized using Tustin's method to produce the frequency response graphs.

A single integrator in C_{11} is adequate for the walking stage to achieve constant average velocities for ramp position references, however, a double integrator in C_{11} is more desirable since it produces zero average WS position errors and, therefore, the shuttle operates about its equilibrium position relative to its frame. In other words, the VCA does not have to correct for a DC offset in the WS position error so the average voice coil current is zero.

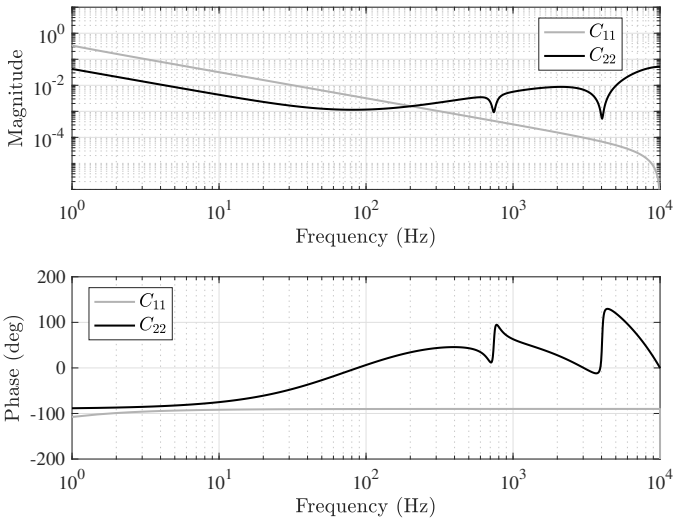

Fig. 9. Frequency responses of C_{11} and C_{22}.

B. Shuttle compensator

Loop shaping is also used to design the C_{22} controller element for P_{22}. It is desirable to design the shuttle loop with as large a bandwidth as practicable since this will provide better rejection of disturbances produced by the walking stage and also dampen the 24 Hz resonance associated with the shuttle. Thus, the following PID filter with two series notch filters at 740 Hz and 4.035 kHz is designed

$$C_{22} = \left(K_{\rm P} + K_{\rm I}\frac{1}{s} + K_{\rm D}\frac{s}{s + \omega_{\rm co}} \right) N_1(s)N_2(s).$$

The PID gains $\{K_{\rm P}, K_{\rm I}, K_{\rm D}\}$, and derivative filter corner frequency $\omega_{\rm co}$ (set to 3 kHz), are selected based on loop shaping arguments. The notch filters, denoted N_1 and N_2, reduce the magnitude of system resonances at frequencies beyond the bandwidth of the loop. An integrator in C_{22} is not necessary for zero average error in the shuttle position because the WS tracks ramp position references with zero average error, however, by including an integrator in the shuttle controller, rejection of low frequency disturbances from sources other than the walking stage is achieved.

The discrete-time controller frequency response is shown in Fig. 9 and the loop gain $P_{22}C_{22}$ is shown in Fig. 10 for the small-signal models. The loop gain is independent of ϕ_0 and a 325 Hz gain crossover is achieved while providing good classical stability margins –the magnitude of the sensitivity function S_{22}, shown in Fig. 7, does not exceed 2.

C. Quantifying rejection of walking stage jitter

The sensitivity function S_{22} shows that perturbations to the shuttle position due to disturbance d_2 are attenuated from DC

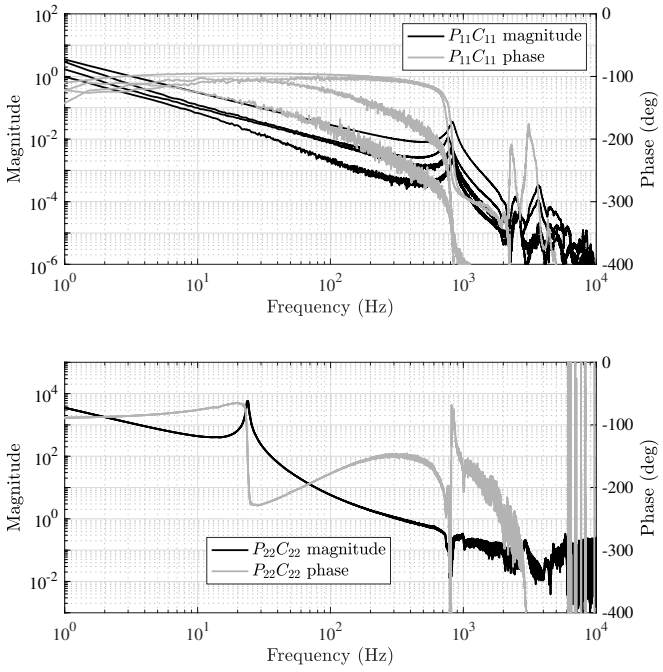

Fig. 10. **Top:** The WS loop gains at the four small-signal frequency responses. The walking stage loop has low bandwidth and is a function of ϕ_0. **Bottom:** The shuttle loop gains at the four small-signal models. The shuttle loop is essentially independent of ϕ_0 with a gain crossover frequency of 325 Hz. See Fig. 7 for the sensitivity function associated with $P_{22}C_{22}$.

to 200 Hz compared to the open-loop system. The shuttle mode near 24 Hz is also effectively dampened. On the other hand, perturbations to the shuttle position in response to disturbances originating from the WS stage (i.e. d_1) are attenuated from DC to 2 kHz. This is demonstrated below.

In open-loop, the short-stroke stage's passive isolation from WS position jitter is determined by $(y_2/u_1)/(y_1/u_1) = P_{21}/P_{11}$, which is the shuttle position normalized by the WS position due to disturbances applied to the WS. The passive isolation attenuates WS disturbances from 34 Hz to 2 kHz as shown in Fig. 7. In closed-loop, the shuttle position normalized by the WS position due to disturbance d_1 is $(y_2/d_1)/(y_1/d_1)$ which is approximated by $(P_{21}/P_{11})S_{22}$ (see (2)), thus, the open-loop transmission, P_{21}/P_{11}, is multiplied by S_{22} which extends the rejection band from DC to 2 kHz.

D. Compensation of periodic error components

The WS position error, e_1, is periodic for constant velocity references and although passive isolation of the shuttle in conjunction with the shuttle feedback loop significantly attenuate WS perturbations, the shuttle tracking error, e_2, exhibits the same periodicity as e_1. The periodic error signals motivate the use of additional filtering of the shuttle tracking error to further reject periodic components in e_2. Among the numerous techniques that are available for reducing periodic errors, modulated-demodulated control (MDC) [33], [34], is well-suited for rejecting the harmonic disturbances experienced by the shuttle because the fundamental frequency of the error

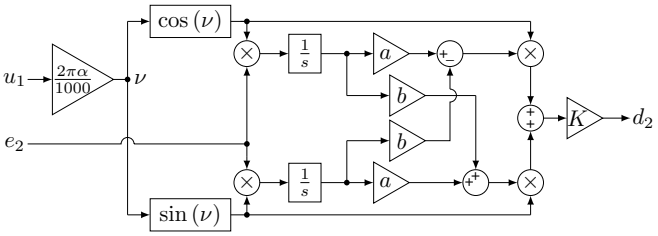

Fig. 11. Block diagram implementation of a controller for rejecting a single frequency harmonic in e_2. Multiple copies targeting different frequencies are arranged in parallel to create C_f.

harmonics is reflected in the period of the output of the low bandwidth WS controller after the modulo operation. The MDC elements are located in C_f in Fig. 8. The signal u_1 provides a timebase for C_f, analogous to a tachometer signal, that the MDC approach exploits to generate the sinusoidal reference signals for demodulating the shuttle tracking error. Regulation of specific harmonics is achieved by appropriately scaling this timebase by an integer multiple. The selection of design parameters is an intuitive loop-shaping process similar to the peak filter design described in [32].

The architecture of a single frequency modulated-demodulated controller is shown in Fig. 11. There are two inputs –the "tachometer" signal, u_1, and the tracking error, e_2. Since one complete period of the PZT legs corresponds to the interval $[0, 1000]$ for u_1, a sinusoid at the fundamental frequency of the legs is generated by selecting the parameter $\alpha = 1$, the second harmonic is generated when $\alpha = 2$, and so forth. The sinusoid blocks in Fig. 11 demodulate the shuttle tracking error e_2 and the integrators act as low-pass filters and compensators whose low frequency output components are combined according to the a and b gains before being modulated back to the harmonic frequency. When tracking ramp position references the output of C_{11} can be assumed to be a ramp βt, with β constant, so that the MDC architecture implements an oscillator with infinite gain at frequency $\omega_0 = 2\pi\alpha\beta/1000$ that is in parallel with C_{22}. The equivalent transfer function from e_2 to d_2 in Fig. 11 is given by

$$K\frac{as + b\omega_0}{s^2 + \omega_0^2}. \tag{3}$$

Closed-loop stability is achieved by appropriate selection of $\{a, b, K\}$ and the process is thoroughly described in [35], however, briefly, if H denotes the closed-loop frequency response e_2/d_2 in Fig. 8, then $\{a, b\}$ are selected so that $\angle(ja + b) + \angle H(\omega_0) = -90^\circ$ while constraining $a^2 + b^2 = 1$ (the phase of the complex number c is denoted $\angle c$). The closed-loop time constant is equal to $\left(\frac{1}{2}|H(\omega_0)|K\right)^{-1}$ and is specified by appropriate choice of K. The final modulated-demodulated controller, C_f, is a sum (parallel connection) of multiple copies of (3). The α's are chosen to target the desired harmonics in the spectrum of e_2 and the convergence rates can be tailored for each harmonic. Thus, the MDC parameters can be tuned based on closed-loop frequency response data.

TABLE III
RMS TRACKING ERRORS FOR RAMP POSITION REFERENCES

Velocity (μm/s)	Walking Stage e_1 (nm)	Shuttle e_2 (nm), $C_\mathrm{f} = 0$	Shuttle e_2 (nm), $C_\mathrm{f} \neq 0$
10	159	1.2	1.2
100	203	2.7	2.3
200	212	5.2	3.5
500	238	13.1	7.0
1000	329	43.0	20.6

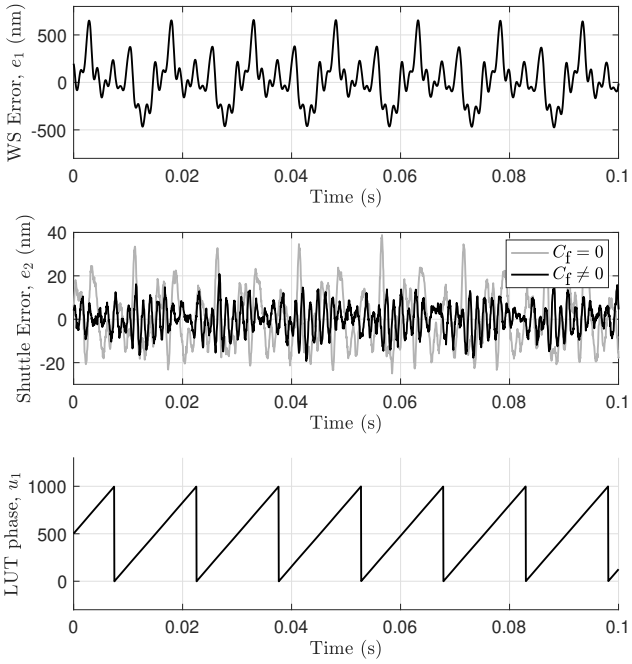

Fig. 12. **Top:** Walking stage tracking error associated with a 0.5 mm/s ramp position reference. **Middle:** The corresponding shuttle tracking errors shown with, and without, C_f. Inclusion of C_f reduces the RMS error by about a factor of two at this velocity. **Bottom:** LUT input generated by the modulo block in Fig. 8. The LUT input is periodic with the same fundamental period as the WS and shuttle errors and is an input to C_f.

IV. Tracking results

A. Continuous scan references

The system is tested with ramp position reference signals corresponding to $\{0.01, 0.1, 0.2, 0.5, 1.0\}$ mm/s velocities – this is analagous to using the positioning system in continuous scan mode. The same reference is provided to the walking stage and shuttle controllers as indicated in Fig. 8. The RMS tracking (position) errors are summarized in Table III. Time-domain examples of the tracking errors for a reference velocity of 0.5 mm/s are graphed in Fig. 12. The case when $C_\mathrm{f} = 0$ is also shown.

When implementing C_f it is necessary to specify the error harmonics to be targeted (based on the selection of α in Fig. 11) and the appropriate gains $\{a, b, K\}$ for each harmonic. With the WS and shuttle loops closed, the plant "H" from the perspective of C_f is shown in Fig. 13. A subset of the tracking error harmonics corresponding to $\alpha = \{2, 4, 6\}$ are selected for all velocities in the $[0.01, 1]$ mm/s range since these α's correspond to the three largest harmonic components in the tracking error. The phases of H at these harmonics are used to determine $\{a, b\}$, and K is selected for each harmonic so that the closed-loop time constants are 0.125 s. The PSDs of e_2 with and without C_f are shown in Fig. 14 when the shuttle's nominal velocity is 0.5 mm/s. The spectrum of e_2 is devoid of any detectible harmonics in a neighborhood of the frequencies $\{126, 252, 378\}$ Hz owing to the unbounded gain of C_f at these frequencies. Table III also summarizes the RMS values of the shuttle position tracking errors when $C_\mathrm{f} \neq 0$.

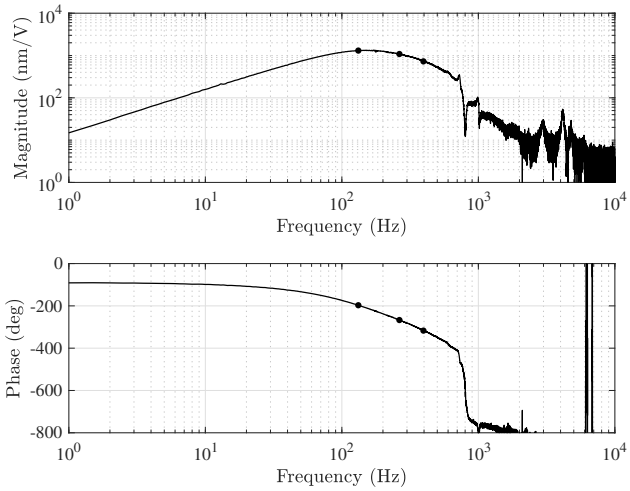

Fig. 13. Frequency response from the perspective of C_f, denoted H. The nominal frequencies of the targeted error harmonics in e_2 for $v_0 = 0.5$ mm/s are marked with "•". See also Fig. 14.

B. Step scanning performance

The system is also tested with step scan references which are of interest when longer exposure times are desired [28]. The shuttle can track step scan references with a 10 ms settling time. For example, Fig. 15 shows the shuttle response to step durations of 50 ms with consecutive step heights of 500 nm. No shaping of the reference signal is implemented for these tests. The walking stage does not track the steps because of its low closed-loop bandwidth but it will (asymptotically) track the average velocity of the step scan profile. The shuttle, however, responds to the sequence of steps and after an initial transient exhibits steady state errors no greater than a few nanometers. The RMS shuttle tracking error is shown in Table IV for a range of step sizes. The RMS error is computed by excluding the 10 ms interval of transient data right after each step, i.e. the 40 ms "dwell" errors are concatenated into a single record and its RMS value is computed. The 2 μm step size requires that the VCA DAC scaling be changed from ± 0.5 V full-scale to ± 2 V full-scale to accommodate the larger errors without saturation.

V. Discussion

RMS tracking errors in the WS are reduced by more than an order of magnitude in the shuttle for constant velocity references less than 1 mm/s with the baseline controller ($C_\mathrm{f} = 0$). The rejection of WS disturbances increases as the

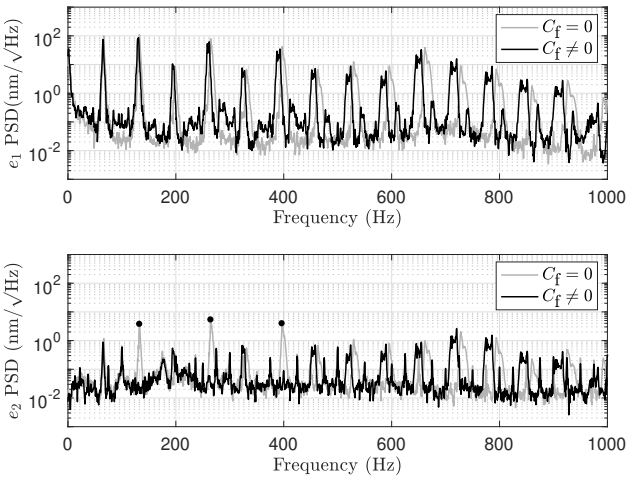

Fig. 14. **Top:** Power spectrum of the walking stage tracking error associated with a 0.5 mm/s ramp position reference. There exist differences in the WS error harmonic frequencies due to variations in how the WS platform responds at different absolute positions of the stage. **Bottom:** Shuttle tracking errors with, and without, C_f. The drift in harmonic frequencies is also passed to the shuttle, however, the modulated-demodulated controller will track drift in the harmonic frequencies due to the incorporation of u_1 into its architecture.

TABLE IV
RMS TRACKING ERRORS FOR STEP SCAN REFERENCES

Step size (nm)	Shuttle, e_2 (nm)
10	1.1
50	1.1
100	1.1
500	1.1
2000†	2.4

† DAC output rescaled

stage velocity decreases –approaching two orders of magnitude for velocities in the 0.01 to 0.1 mm/s range –because the disturbance spectrum is more fully contained within the shuttle controller bandwidth. Disturbance rejection is further improved when the three dominant harmonics in e_2 are targeted by C_f, especially in the higher velocity cases where a factor of two reduction in RMS error is observed compared to the baseline controller. Compensating additional harmonics with the MDC filter is possible, however, DSP computational limitations currently restrict the number of harmonics to three in the present hardware. Variation in the WS disturbance fundamental frequency is also observed as the WS moves at a constant velocity over its entire stroke. Using u_1 to generate the modulation/demodulation sinusoids of the MDC filter, however, adapts the output of C_f to exactly match the harmonic frequencies in the WS jitter.

The synergism of the feedback controller *with* the passive isolation created by the low stiffness flexures enables the large reduction in the shuttle tracking error. If the short-stoke stage had been designed with a stiff actuator, such as a piezoelectric element, then walking stage position errors would be more readily transmitted to the shuttle which would require that the shuttle loop have a higher gain crossover frequency leading to potentially more coupling between the shuttle controller

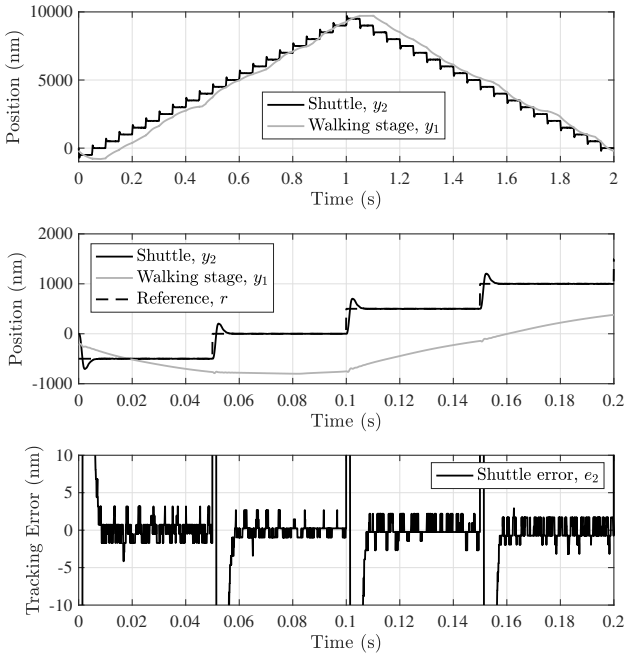

Fig. 15. **Top:** Absolute positions of the WS and shuttle in response to a step scan reference signal with 500 nm steps and 50 ms dwell period. **Middle:** Position details and reference. The shuttle overshoot is 35% with a 10 ms settling time. **Bottom:** Shuttle position tracking error, computed by subtracting the shuttle position from the step scan reference signal.

and WS dynamics. The proposed system avoids this since the shuttle loop is essentially independent of the walking stage dynamics. This imparts additional robustness to changes in the WS. One potential drawback of the proposed system is that direct disturbances to the shuttle must be within the force limits of the VCA since they are not opposed by a stiff actuator.

Finally, the suitability of the proposed system for FTS applications is addressed. Comparing Tables I and III, it is concluded that the RMS shuttle error must be further reduced by a factor of four across all of the bands in Table I in order to meet the requirements of a Fourier transform spectrometer that covers the visible spectrum. A path to achieve the error reduction may be possible with further optimization of the short-stroke stage to reduce its resonant frequency, however, the shuttle metrology will need to be improved to sub-nanometer resolution.

VI. Conclusion

The proposed dual-stage system is under development for application in compact spaceborne Fourier transform spectrometers. Walking stages are excellent choices for the long-stroke stage due to their high resolution point-to-point positioning capability, however, they are less suited for tracking non-constant reference signals. The short-stroke stage using a voice-coil-actuated shuttle has been demonstrated to significantly reduce tracking errors in the shuttle position in response to ramp position references. The design rationale to employ low stiffness flexures in the secondary stage and the inclusion of a modulated-demodulated control scheme to compensate repetitive errors are validated by the experimental results.

VII. Acknowledgements

The authors thank the Jet Propulsion Laboratory SURP program for supporting this research. The authors are also grateful to Fadi Rafidi for assisting with the fabrication of the short-stroke stage.

References

[1] S. P. Davis, M. C. Abrams, and J. W. Brault, *Fourier Transform Spectroscopy*. Academic Press, 2001.

[2] V. Saptari, *Fourier-Transform Spectroscopy Instrumentation Engineering*, A. Weeks, Ed. SPIE, 2004, vol. TT61.

[3] F. Grandmont, H. Buijs, and J. Mandar, "Interferometer scanning mechanisms and metrology at ABB: recent developments and future perspectives," in *International Conference on Space Optics, ICSO 2014*, Z. Sodnik, B. Cugny, and N. Karafolas, Eds., vol. 10563, International Society for Optics and Photonics. SPIE, 2017, pp. 1132–1137.

[4] V. Natraj *et al.*, "Simulated multispectral temperature and atmospheric composition retrievals for the JPL GEO-IR Sounder," *Atmospheric Measurement Techniques*, vol. 15, no. 5, pp. 1251–1267, 2022.

[5] J. A. Kramar, "Nanometre resolution metrology with the molecular measuring machine," *Meas. Sci. Technol.*, vol. 16, no. 11, pp. 2121–2128, 2005.

[6] L. Chassagne, M. Wakim, S. Xu, S. Topçu, P. Ruaux, P. Juncar, and Y. Alayli, "A 2D nano-positioning system with sub-nanometric repeatability over the millimetre displacement range," *Meas. Sci. Technol.*, vol. 18, no. 11, pp. 3267–3272, 2007.

[7] A. Sinno, P. Ruaux, L. Chassagne, S. Topçu, Y. Alayli, G. Lerondel, S. Blaize, A. Bruyant, and P. Royer, "Enlarged atomic force microscopy scanning scope: Novel sample-holder device with millimeter range," *Rev. Sci. Instrum.*, vol. 78, no. 9, pp. 1–7, September 2007.

[8] Y. K. Yong, S. O. R. Moheimani, B. J. Kenton, and K. K. Leang, "High-speed flexure-guided nanopositioning: Mechanical design and control issues," *Review of Scientific Instruments*, vol. 83, no. 12, p. 121101, 2012.

[9] B. J. Kenton and K. K. Leang, "Design and control of a three-axis serial-kinematic high-bandwidth nanopositioner," *IEEE/ASME Trans. Mechatronics*, vol. 17, no. 2, pp. 356–369, 2012.

[10] T. Tuma, W. Haeberle, H. Rothuizen, J. Lygeros, A. Pantazi, and A. Sebastian, "Dual-stage nanopositioning for high-speed scanning probe microscopy," *IEEE/ASME Trans. Mechatronics*, vol. 19, no. 3, pp. 1035–1045, 2014.

[11] Y. K. Yong, S. S. Aphale, and S. O. R. Moheimani, "Design, identification, and control of a flexure-based xy stage for fast nanoscale positioning," *IEEE Transactions on Nanotechnology*, vol. 8, no. 1, pp. 46–54, 2009.

[12] H. Zhu and H. Fujimoto, "Mechanical deformation analysis and high-precision control for ball-screw-driven stages," *IEEE/ASME Trans. Mechatronics*, vol. 20, no. 2, pp. 956–966, 2015.

[13] E. S. Buice, D. Otten, R. H. Yang, S. T. Smith, R. J. Hocken, and D. L. Trumper, "Design evaluation of a single-axis precision controlled positioning stage," *Precision Engineering*, vol. 33, no. 4, pp. 418–424, 2009.

[14] X. Shan, S.-K. Kuo, J. Zhang, and C.-H. Menq, "Ultra precision motion control of a multiple degrees of freedom magnetic suspension stage," *IEEE/ASME Trans. Mechatronics*, vol. 7, no. 1, pp. 67–78, 2002.

[15] W.-j. Kim and S. Verma, "Multiaxis maglev positioner with nanometer resolution over extended travel range," *J. Dyn. Sys. Meas. Control.*, vol. 129, no. 6, pp. 777–785, November 2007.

[16] X. Li, H. Zhu, J. Ma, T. J. Teo, C. S. Teo, M. Tomizuka, and T. H. Lee, "Data-driven multiobjective controller optimization for a magnetically levitated nanopositioning system," *IEEE/ASME Trans. Mechatronics*, vol. 25, no. 4, pp. 1961–1970, 2020.

[17] V. H. Nguyen and W.-j. Kim, "Two-phase Lorentz coils and linear Halbach array for multiaxis precision-positioning stages with magnetic levitation," *IEEE/ASME Trans. Mechatronics*, vol. 22, no. 6, pp. 2662–2672, 2017.

[18] P. Berkelman and M. Dzadovsky, "Magnetic levitation over large translation and rotation ranges in all directions," *IEEE/ASME Trans. Mechatronics*, vol. 18, no. 1, pp. 44–52, 2013.

[19] T. Hu and W.-j. Kim, "Extended range six-dof high-precision positioner for wafer processing," *IEEE/ASME Trans. Mechatronics*, vol. 11, no. 6, pp. 682–689, 2006.

[20] V. H. Nguyen and W.-j. Kim, "Design and control of a compact lightweight planar positioner moving over a concentrated-field magnet matrix," *IEEE/ASME Trans. Mechatronics*, vol. 18, no. 3, pp. 1090–1099, 2013.

[21] H. Chen, M. Zhang, H. Mu, Y. Zhu, C. Hu, and T. Cai, "Conceptual design and trajectory planning of a precision repetitive-scanning stage with separated drive unit for energy saving," *IEEE/ASME Trans. Mechatronics*, vol. 21, no. 4, pp. 2142–2153, 2016.

[22] H. Zhu, T. J. Teo, and C. K. Pang, "Magnetically levitated parallel actuated dual-stage (Maglev-PAD) system for six-axis precision positioning," *IEEE/ASME Trans. Mechatronics*, vol. 24, no. 4, pp. 1829–1838, 2019.

[23] Y.-M. Choi and D.-G. Gweon, "A high-precision dual-servo stage using Halbach linear active magnetic bearings," *IEEE/ASME Trans. Mechatronics*, vol. 16, no. 5, pp. 925–931, 2011.

[24] M. Li, Y. Zhu, K. Yang, and C. Hu, "A data-driven variable-gain control strategy for an ultra-precision wafer stage with accelerated iterative parameter tuning," *IEEE Transactions on Industrial Informatics*, vol. 11, no. 5, pp. 1179–1189, 2015.

[25] M. Li, Y. Zhu, K. Yang, C. Hu, and H. Mu, "An integrated model-data-based zero-phase error tracking feedforward control strategy with application to an ultraprecision wafer stage," *IEEE Transactions on Industrial Electronics*, vol. 64, no. 5, pp. 4139–4149, 2017.

[26] G. Parmar, K. Barton, and S. Awtar, "Large dynamic range nanopositioning using iterative learning control," *Precision Engineering*, vol. 38, no. 1, pp. 48–56, 2014.

[27] Q. Xu, "Design and development of a compact flexure-based xy precision positioning system with centimeter range," *IEEE Transactions on Industrial Electronics*, vol. 61, no. 2, pp. 893–903, 2014.

[28] L. Drissen *et al.*, "SITELLE: an Imaging Fourier Transform Spectrometer for the Canada-France-Hawaii Telescope," *Monthly Notices of the Royal Astronomical Society*, vol. 485, no. 3, pp. 3930–3946, 03 2019.

[29] R. J. E. Merry, N. C. T. de Kleijn, M. J. G. van de Molengraft, and M. Steinbuch, "Using a walking piezo actuator to drive and control a high-precision stage," *IEEE/ASME Trans. Mechatronics*, vol. 14, no. 1, pp. 21–31, 2009.

[30] R. J. E. Merry, J. L. Holierhoek, M. J. G. van de Molengraft, and M. Steinbuch, "Gain scheduling control of a walking piezo actuator," *IEEE/ASME Trans. Mechatronics*, vol. 19, no. 3, pp. 954–962, 2014.

[31] R. Saathof, M. Thier, R. Hainisch, and G. Schitter, "Integrated system and control design of a one DoF nano-metrology platform," *Mechatronics*, vol. 47, pp. 88–96, 2017.

[32] E. Csencsics, M. Thier, S. Ito, and G. Schitter, "Supplemental peak filters for advanced disturbance rejection on a high precision endeffector for robot-based inline metrology," *IEEE/ASME Trans. Mechatronics*, vol. 27, no. 4, pp. 2258–2266, 2022.

[33] K. Lau, G. C. Goodwin, and R. T. M'Closkey, "Properties of modulated and demodulated systems with implications to feedback limitations," *Automatica*, vol. 41, no. 12, pp. 2123–2129, Oct 2005.

[34] A. Bazaei and S. R. Moheimani, "Synthesis of modulated-demodulated control systems," *Automatica*, vol. 50, no. 7, pp. 1816–1824, 2014.

[35] C. Hendrickson and R. T. M'Closkey, "Compensation of nonlinear harmonic coupling for pulsed-jet-velocity shaping," *AIAA J.*, vol. 51, no. 11, pp. 1–15, Nov 2013.